JOURNAL OF GUIDANCE, CONTROL, AND DYNAMICS
Vol. 16, No. 6, November–December 1993

Fuel-Optimal Slewing of an Experimental Hinged-Free Beam

Larry Silverberg* and John L. Meyer†
North Carolina State University, Raleigh, North Carolina 27695

With the recent development of numerical methods for exactly solving larger order fuel-optimal control problems, the implementation of exact real-time fuel-optimal control becomes possible. This paper describes a physical experiment in which a hinged-free beam is slewed in a fuel-optimal manner. A comparison between experimental results and the analytical predictions highlights the sources of errors typical of this class of problems.

I. Introduction

HISTORICALLY, the exact solutions of fuel-optimal control problems have been obtained analytically, which has limited exact solutions to linear systems of relatively low order ($n \leq 3$).[1] Recently, a numerical procedure for exactly solving fuel-optimal control problems was developed.[2] The savings in fuel provided by the exact solution over approximating techniques can be on the order of 20–50%.[3,4] Whereas a great many approximating techniques have been implemented in physical experiments,[5-8] this paper describes for the first time the implementation of the exact fuel-optimal solution in a physical experiment.

The physical setup consists of a spring steel beam fastened to a hinged aluminum mount, two air thrust actuators, an angular rate sensor located on the mount, and a strain gauge located at the root of the beam. The system parameters are given in Table 1. The setup is shown in Fig. 1.

The next section describes the beam dynamics. The associated equations of motion were derived with the aid of floating coordinates.[9] The use of floating coordinates decouples the rigid-body motion and elastic motion. Section III reviews the formulation of the fuel-optimal control problem. It is interesting to note that the solution was obtained by geometric constructs rather than by calculus of variations. Section IV describes the air thrust actuation. The calibration of the air thrust actuation force is described along with the procedure in which instantaneous impulses are converted into finite time pulses. Section V describes the construction of the elastic displacement profile from the strain gauge measurements. Section VI discusses the angular rate measurement. Section VII describes the experimental results. Reconstructed modal response measurements are compared with analytical predictions of the modal responses, natural frequencies are identified, and the nature of the fuel-optimal solution is discussed. Finally, the results are discussed in Sec. VIII.

II. Beam Dynamics

The dynamics of the hinged-free beam are represented by the differential equations of motion

$$J\ddot{\theta}(t) = T(t) = u_1(t)x_1 + u_2(t)x_2 \tag{1}$$

$$\rho(x)\frac{\partial^2 w(x,t)}{\partial t^2} + C\frac{\partial w(x,t)}{\partial t} + \frac{\partial^2}{\partial x^2}\left[EI\frac{\partial^2 w(x,t)}{\partial x^2}\right] = u_1(t)\delta(x-x_1) + u_2(t)\delta(x-x_2) \qquad (0<x<L) \tag{2}$$

subject to the boundary conditions

$$w(0,t) = \frac{\partial^2 w(0,t)}{\partial x^2} = \frac{\partial^2 w(L,t)}{\partial x^2} = \frac{\partial}{\partial x}\left[EI\frac{\partial^2 w(L,t)}{\partial x^2}\right] = 0$$

in which $w(x, t)$ denotes the elastic displacement of the beam at point x and time t. As shown in Fig. 2, the elastic displacement is measured relative to a floating coordinate system that coincides with the rigid-body slewing motion of the beam.[9] The rigid-body slewing angle is denoted by $\theta(t)$ and the applied torque is denoted by $T(t)$. The mass moment of inertia about the hinge point is denoted by J, the mass per unit length by $\rho(x)$, the stiffness by $EI(x)$, and the structural damping operator by C. The damping operator, which includes both struc-

Table 1 System parameters

Component	Parameter	Symbol	Value
Beam	Length, in.	L_b	60.0
	Width, in.		3.0
	Thickness, in.	T	0.064
	Elastic modulus, in.^{2}	E_b	24.25×10^{-6}
	Area moment of inertia, in.^{4}	I_b	6.554×10^{-5}
	Mass per unit length, slug/ft	ρ_b	0.022
	Structural damping, s^{-1}	$2\zeta\omega_1$	0.15
Mount	Length, in.	L_m	11.8125
	Width, in.		5.0
	Thickness, in.		0.5
	Elastic modulus, in.^{2}	E_m	10×10^{-6}
	Area moment of inertia, in.^{4}	I_m	5.2083×10^{-2}
	Mass per unit length, slug/ft	ρ_m	0.20
Air thrust actuators	Locations, in.	x_1	31.044
		x_2	61.284
	Masses, slug	m_1	0.01276
		m_2	0.01274
Angular rate transducer	Location, in.	—	4.50
	Mass, slug	—	0.02525
Strain gauge	Location, in.	x_m	11.8125
	Mass	—	0.0

Received Oct. 3, 1992; revision received Feb. 26, 1993; accepted for puyblication March 12, 1993.

*Associate Professor, Department of Mechanical and Aerospace Engineering, and Mars Mission Research Center. Member AIAA.
†Graduate Research Assistant, Mars Mission Research Center. Student Member AIAA.

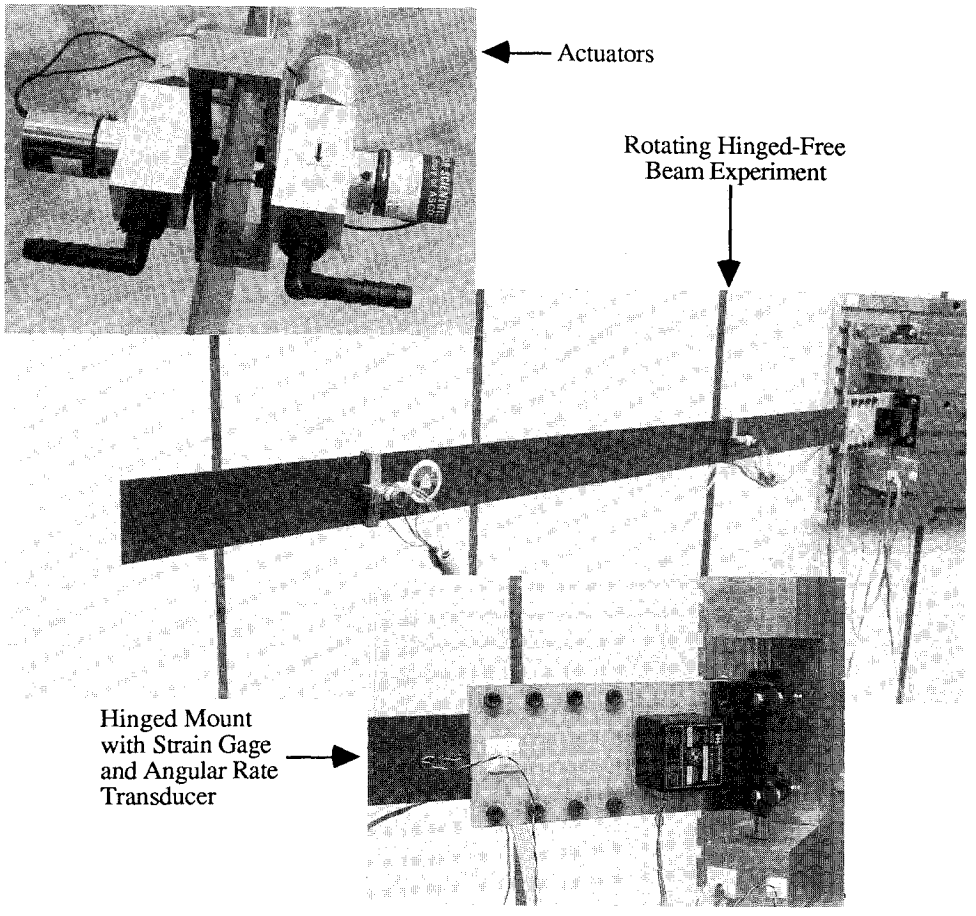

Fig. 1 Setup.

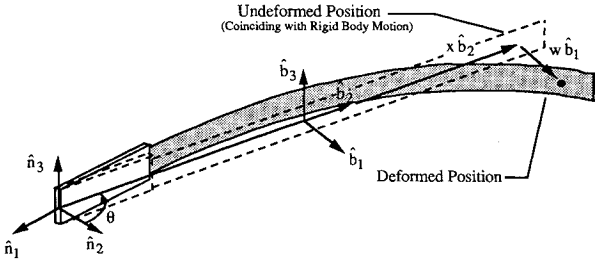

Fig. 2 Coordinate systems.

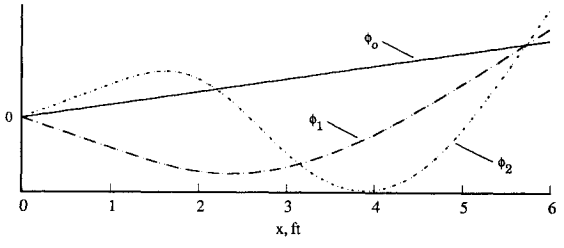

Fig. 3 Lowest three modes of a hinged-free beam.

tural damping and air damping, is of the proportional type, thereby preserving the normal mode characteristics of the vibration. This assumption is quite reasonable in the case of light damping.

The air thrust actuators apply point forces $u_1(t)$ and $u_2(t)$, and the corresponding spatial impulse functions are $\delta(x - x_1)$ and $\delta(x - x_2)$, respectively. The normal modes and frequencies of the system are computed by solving the associated eigenvalue problem

$$\omega_r^2 \rho(x)\phi_r(x) = \frac{d^2}{dx^2}\left[EI\frac{d^2\phi_r(x)}{dx^2}\right], \qquad (r = 0, 1, 2, \ldots)$$

subject to the boundary conditions just indicated. After one arranges the modes $\phi_r(x)$ and corresponding frequencies ω_r in ascending order, the lowest mode is the rigid-body slewing mode denoted by $\phi_0(x)$, and the associated frequency is zero ($\omega_0 = 0$). The second mode is the fundamental elastic mode denoted by $\phi_1(x)$ and the associated fundamental frequency is denoted by ω_1. The solution of the eigenvalue problem is obtained by the Rayleigh-Ritz method using the admissible functions

$$\psi_r(x) = \frac{x}{2L}\left[1 + \left(\frac{x}{L}\right)^{r-1}\right], \qquad (r = 1, 2, \ldots, 12)$$

The associated mass and stiffness matrices are[10]

$$m_{rs} = \rho_m \int_0^{x_m} \psi_s(x)\psi_r(x)\,dx + \rho_b \int_{x_m}^{x_t} \psi_s(x)\psi_r(x)\,dx$$

$$k_{rs} = E_m I_m \int_0^{x_m} \psi_s''(x)\psi_r''(x)\,dx + E_b I_b \int_{x_m}^{x_t} \psi_s''(x)\psi_r''(x)\,dx$$

The lowest three modes are shown in Fig. 3. Note that the two air thrust actuators were placed at the two nodes of the third mode to eliminate control spillover into that mode. The placement of the two actuators was an iterative process as a consequence of the effect of the actuator mass on the nodal locations.

Neglecting the influence of the second and higher elastic modes, the elastic displacement has the form

$$w(x, t) = \phi_1(x)q_1(t) \tag{3}$$

where $q_1(t)$ is the fundamental modal displacement. Substituting Eq. (3) into Eq. (2), premultiplying by $\phi_1(x)$, and integrating over the domain, one transforms Eq. (2) into the modal equation of motion[9]

$$\ddot{q}_1(t) = -2\zeta\omega_1\dot{q}_1(t) - \omega_1^2 q_1(t) + \phi_1(x_1)u_1(t) + \phi_1(x_2)u_2(t) \tag{4}$$

where ζ is the damping factor. Equations (1) and (4) are recast in the form of the linear state equations

$$\dot{x}(t) = Ax(t) + Bu(t) \tag{5}$$

where $x(t) = [\theta(t)\ \dot{\theta}(t)\ q_1(t)\ \dot{q}_1(t)]^T$, $u(t) = [u_1(t)\ u_2(t)]^T$,

$$A = \begin{bmatrix} 0 & 1 & 0 & 0 \\ 0 & 0 & 0 & 0 \\ 0 & 0 & 0 & 1 \\ 0 & 0 & -\omega_1^2 & -2\zeta\omega_1 \end{bmatrix} \tag{6a}$$

$$B = \begin{bmatrix} 0 & 0 \\ x_1/J & x_2/J \\ 0 & 0 \\ \phi_1(x_1) & \phi_1(x_2) \end{bmatrix} \tag{6b}$$

The solution to Eq. (5) is

$$x(t) = e^{At}\left[x(0) + \int_0^t e^{-As}Bu(s)\,ds\right] \tag{7}$$

where

$$e^{-At} = \begin{Bmatrix} 1 & -t & 0 & 0 \\ 0 & 1 & 0 & 0 \\ 0 & 0 & e^{\zeta\omega_1 t}\left[\cos(\omega_d t) - \frac{\zeta\omega_1}{\omega_d}\sin(\omega_d t)\right] & -\frac{1}{\omega_d}e^{\zeta\omega_1 t}\sin(\omega_d t) \\ 0 & 0 & \frac{\omega_1}{\omega_d}e^{\zeta\omega_1 t}\sin(\omega_d t) & e^{\zeta\omega_1 t}\left[\cos(\omega_d t) + \frac{\zeta\omega_1}{\omega_d}\sin(\omega_d t)\right] \end{Bmatrix} \tag{8}$$

in which $\omega_d = \omega_1\sqrt{1-\zeta^2}$.

III. Fuel-Optimal Control

The objective of the control is to transfer the system from the initial state $x_0 = x(0)$ to the final state $x_1 = x(T_f)$ in maneuver time T_f. The fuel function associated with propulsive actuation is

$$\text{fuel} = \sum_{j=1}^{2}\int_0^{T_f}|u_j(t)|\,dt \tag{9}$$

The fuel-optimal control transfers x_0 to x_1 in maneuver time T_f while minimizing the fuel.

The development of the fuel optimal control solution is rooted in set theory and beyond the scope of this paper. Thus, the details of this development have been omitted, leaving only the necessary results.[1-4] The control determining functions are defined as

$$g_j(\eta, t) = \eta^T e^{-At}b_j, \qquad (j = 1, 2) \tag{10}$$

where $B = [b_1\ \ b_2]$. Here η is a 4×1 vector contained in the hyperplane

$$H = (\eta : \eta^T y = 1) \tag{11}$$

where $y = e^{-AT_f}x_1 - x_0$. The vector η is called the normal vector. Optimal control problems in general reduce to selecting a particular normal vector η from the hyperplane H. In the case of fuel-optimal control, we define the fuel coefficient

$$\alpha^* = \min_{\eta\in H}\max_{j=1,2}\sup_{0\le t\le T_f}|g_j(\eta, t)| \tag{12}$$

The solution of Eq. (12) uniquely yields the optimal normal vector η^*. The fuel-optimal controls are of the form

$$u_j^*(t) = g_j^T c_j/\alpha^*, \qquad (j = 1, 2) \tag{13}$$

in which g_j is an $N_j \times 1$ vector of impulses and c_j is an $N_j \times 1$ vector of impulse coefficients, given by

$$g_j = \{\text{sgn}[g_j(\eta^*,\tau_{1j})]\delta(t-\tau_{ij})\cdots\text{sgn}[g_j(\eta^*,\tau_{N_jj})]\delta(t-\tau_{N_jj})\}^T \tag{14a}$$

$$c_j = [c_{1j}\quad c_{2j}\quad \cdots\quad c_{N_jj}]^T \tag{14b}$$

The jth fuel-optimal control input $u_j^*(t)$ represents a series in time of N_j impulses. Here N_j $(j = 1, 2)$ corresponds to the multiple solutions to Eq. (12), $\alpha^* = |g_j(\eta^*,\tau_{ij})|$ $(i = 1, 2, \ldots, N_j; j = 1, 2)$. Note that N_j may be equal to zero for some j if $g_j(\eta^*,t)$ does not assume the value of α^* at any time during the maneuver. In this case, $u_j^*(t) = 0$. The impulse coefficients c_{ij} given in Eq. (14b) are nonnegative constants that satisfy

$$1 = \hat{1}^T c \tag{15}$$

where

$$c = [c_1^T\quad c_2^T]^T \tag{16a}$$

$$\hat{1} = [1\quad 1\quad \cdots\quad 1]^T \tag{16b}$$

The impulse coefficients are chosen so that the resulting control accomplishes the stated objective, that is, such that the system is transferred from x_0 to x_1 in time T_f. In some cases, multiple solutions exist. Substituting Eq. (13) into Eq. (9), one finds that the minimal amount of fuel is

$$\text{fuel}^* = 1/\alpha^* \tag{17}$$

The slewing maneuver is defined by $x_0 = [\theta_0\ 0\ 0\ 0]^T$ and $x_1 = 0$, which reduces the hyperplane constraint, Eq. (11), to

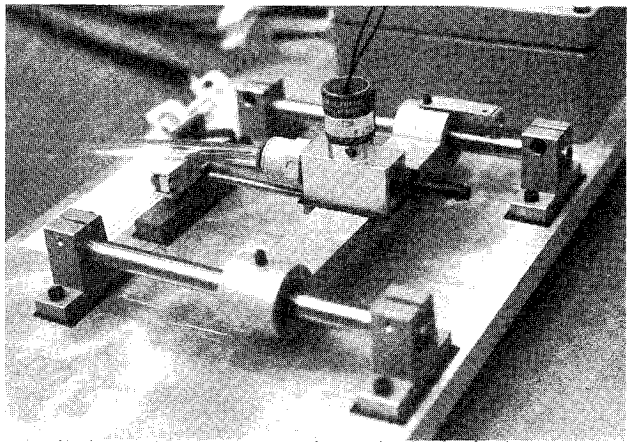

Fig. 4 Air thrust calibration and characterization experiment.

Table 2 Typical air thrust actuator parameters ($P_s = 50$ psi)

Peak overshoot, %	140
Delay time, s	0.003
Rise time, s	0.010
Peak time, s	0.014
Settling time, s	0.090
Drop off time, s	0.006

$\eta_1 = -1/\theta_0$. From Eqs. (6), (8), and (10), the control-determining functions are explicitly

$$g_1(\eta, t) = \frac{x_1 t}{J\theta_0} + \frac{x_1}{J}\eta_2 - \frac{\phi_1(x_1)e^{\zeta\omega_1 t}\sin(\omega_d t)}{\omega_d}\eta_3 + \phi_1(x_1)e^{\zeta\omega_1 t}\left[\cos(\omega_d t) + \frac{\zeta\omega_1}{\omega_d}\sin(\omega_d t)\right]\eta_4 \quad (18a)$$

$$g_2(\eta, t) = \frac{x_2 t}{J\theta_0} + \frac{x_2}{J}\eta_2 - \frac{\phi_1(x_2)e^{\zeta\omega_1 t}\sin(\omega_d t)}{\omega_d}\eta_3 + \phi_1(x_2)e^{\zeta\omega_1 t}\left[\cos(\omega_d t) + \frac{\zeta\omega_1}{\omega_d}\sin(\omega_d t)\right]\eta_4 \quad (18b)$$

IV. Air Thrust Actuation

The actuator thrust was measured as a function of supply line pressure via the calibration experiment depicted in Fig. 4. The test apparatus consisted of an actuator fastened to two precision linear bearings riding on hardened steel rods. A load introduction bolt transmitted the actuator output to a 0.5-kg load cell. Air thrust activation timing and measurement were controlled by an Intel 80386 based microcomputer system that allowed for high data collection rates relative to the beam's lowest three frequencies of oscillation. System characteristics determined from the calibration experiment are shown in Figs. 5 and 6 and Table 2.[11] Three sets of actuator test data were taken at each supply pressure level to determine steady-state thrust levels. The order of the tests was randomized to minimize any trend effects. The data, as shown in Fig. 6, were modeled by the equation

$$F = 1.681753 \times 10^{-3} * P_s + 1.249038 \times 10^{-5} * P_s^2 \qquad 10 < P_s < 100 \quad (19)$$

where F is the thrust of each actuator in pounds force and P_s is the supply pressure in pounds per square inch.

The implementation of fuel-optimal control, as it was formulated in the previous section, requires instantaneous impulses to be converted into finite time pulses of duration Δt. The duration of the pulse is determined such that the magnitudes of the instantaneous impulse and of the pulse are equal. Thus the ith pulse produced by actuator j, denoted by F_{ij}, is defined such that

$$\int_{T_{1ij}}^{T_{2ij}} F_{ij}\,dt = \int_{T_{1ij}}^{T_{2ij}} \frac{c_{ij}}{\alpha^*} \cdot \mathrm{sgn}[g_j(\eta^*, \tau_{ij})]\delta(t - \tau_{ij})\,dt = \frac{c_{ij}}{\alpha^*} \quad (20)$$

where

$$\Delta t_{ij} = T_{2ij} - T_{1ij}$$

From Eq. (20), the equivalent pulse duration Δt_{ij} is defined by

$$\Delta t_{ij} = c_{ij}/\alpha^* \cdot F_{ij} \quad (21)$$

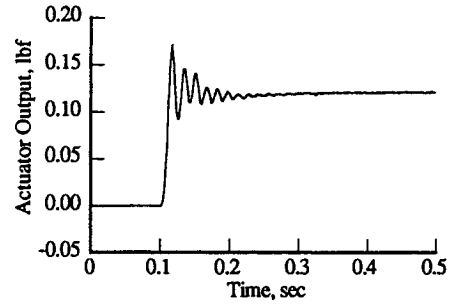

Fig. 5 Typical air thrust response to supply line pressure step input (0.1-s input delay).

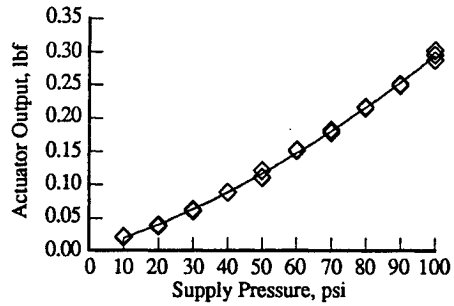

Fig. 6 Air thrust vs supply pressure.

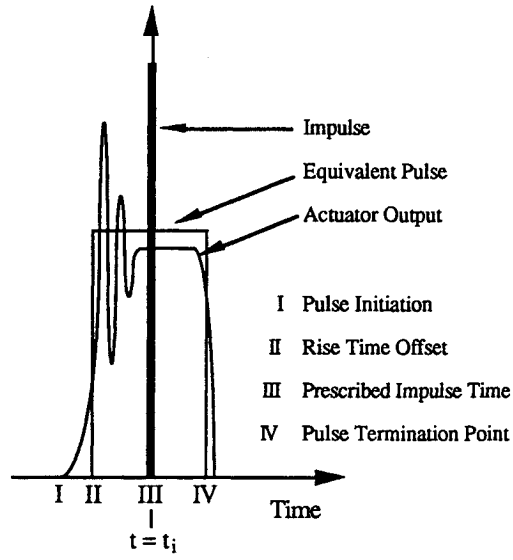

Fig. 7 Equivalent air thrust pulse.

Table 3 Comparison of predicted and measured natural frequencies (rad/s)

Frequency	Predicted	Measured
ω_1	1.34	1.31
ω_2	4.93	4.93

Table 4 Impulse times and magnitudes

Impulse time, s	Impulse coefficient	Direction
0.000000000000000	0.499831142213645	−
5.501674167355190	0.214237597126137	+
6.000000000000000	0.285593545087508	+

The time at which the pulse is initiated, T_{1ij}, depends on the prescribed impulse time τ_{ij}, the rise time of the actuators t_r, and the equivalent pulse duration Δt_{ij}. We obtain

$$T_{1ij} = \tau_{ij} - t_r - (\Delta t_{ij}/2) \tag{22}$$

The final term in Eq. (22) centers the pulse over its prescribed impulse time. The result of Eq. (22) is illustrated in Fig. 7. Not indicated in Eq. (22), when the first pulse initiates the maneuver (at $t = 0$) the pulse cannot be centered. To compensate, each successive pulse after the first is delayed by half the duration of the first pulse.

V. Strain Measurement

The open-loop fuel-optimal control solution does not require measurements of the states. However, measurements of the states were performed for purposes of comparison with the analytical predictions. Indeed, all of the states can be extracted from the strain measurement and the angular rate measurement.

A strain gauge was placed where the beam joins the mount. The gauge was thin, flexible, and self-temperature compensating. A high resistance of 350 Ω was selected to increase the signal-to-noise ratio. The transverse sensitivity was low ($0.8 \pm 0.2\%$) to reduce the corruption of the pure bending component by torsional effects. The elastic displacement of the beam relative to a line tangent to the beam at its root is expressed in the form of a cubic function $w_m(x, t)$, and we impose the boundary conditions

$$w_m(0, t) = \frac{\partial w_m(0, t)}{\partial x} = \frac{\partial^2 w_m(L, t)}{\partial x^2} = 0$$

and

$$\frac{\partial^2 w_m(0, t)}{\partial x^2} = \Gamma(t)$$

where $\Gamma(t)$ is the beam curvature at the root. We obtain the form

$$w_m = -\frac{\Gamma}{6L}x^3 - \frac{\epsilon}{T}x^2, \qquad \Gamma = -\frac{2\epsilon}{T} \tag{23}$$

where $\epsilon = \epsilon(t)$ is the measured strain. The time rate of change of $w_m(x, t)$ was computed by a backward finite difference.

VI. Angular Rate Measurement

The angular rate transducer located on the mount provided voltage output linearly proportional to the angular rate input. Hysteresis was essentially zero with a slow transient shift of the null signal typically ± 1% of full scale. The 12-bit data acquisition restricted input resolution to 1.221×10^{-3} deg/s. The unit threshold was approximately 0.01 deg/s with a maximum measured rate of 180 deg/s. Angular position measurements were extracted by numerical integration.

VII. Experimental Results

The analytically predicted natural frequencies and the measured natural frequencies are compared in Table 3. The experimentally measured frequencies were obtained by imparting initial conditions on the structure that excited the rigid-body mode and several flexible-body modes. Free response angular rate measurements were used to calculate the power spectral density shown in Fig. 8.

The modal coordinates are extracted from the measured quantities in a procedure that was generalized for maneuvering elastic bodies in Ref. 12. More specifically, we can transform the measured quantities into modal quantities from Fig. 9. We obtain

$$\theta(t) = \theta_m(t) - \frac{1}{x_c}\left[\frac{1}{M}\int_0^L \rho(x) w_m(x, t)\, dx\right] \tag{24}$$

$$w(x, t) = w_m(x, t) - \frac{x}{x_c}\left[\frac{1}{M}\int_0^L \rho(x) w_m(x, t)\, dx\right] \tag{25}$$

where $x_c = 19.94$ in. denotes the position of the mass center, $M = 0.358$ slugs denotes the total mass, $\theta_m(t)$ is the measured angle, and Eq. (23) is substituted into the integral terms before they are evaluated.

The hinged-free beam is slewed 35 deg in 6 s. The numerical solution of the fuel-optimal control problem[2] yields

$$\alpha^* = 12.389098861099480, \qquad \text{fuel} = 0.08071612078 \tag{26}$$

and the optimal normal vector

$$\tilde{\eta} = \begin{bmatrix} -1.637022271802352 \\ -4.894758065691531 \\ -3.000156016538542 \\ 0.195758065691530 \end{bmatrix}$$

The phase plane plot of the rigid-body rotation angle $\theta(t)$ is shown in Fig. 10. The phase plane plot of the modal coordi-

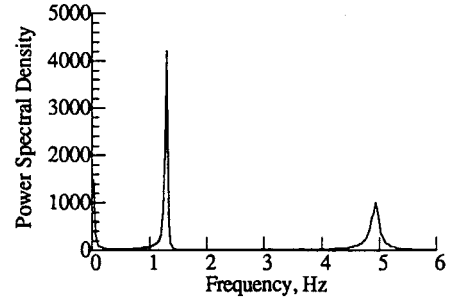

Fig. 8 Measured natural frequencies.

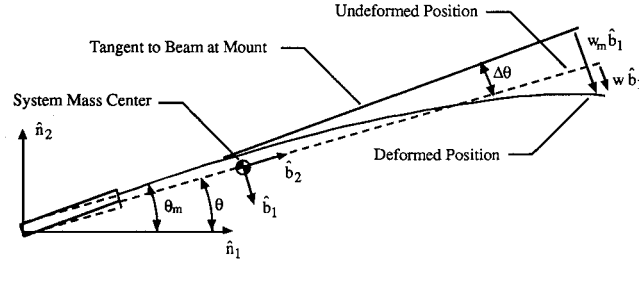

Fig. 9 Modal transformation.

nate $q_1(t)$ is shown in Fig. 11. Note that $q_1(t)$ was obtained by substituting Eq. (25) into Eq. (3) and evaluating the result at the beam tip. The impulse times and impulse coefficients were computed using the numerical technique developed in Ref. 2. The inner actuator was determined to have no impulses. The impulse times and impulse coefficients of the outer actuator are given in Table 4.

VIII. Discussion

The analytical results are shown in Figs. 10 and 11, and the experimental results are shown in Figs. 12 and 13. There were two significant sources of error in this experiment: modeling and actuator dynamics. The modeling errors included system mass moment of inertia, fundamental frequency of oscillation, and actuator placement. An inaccurate estimate of the moment of inertia would prevent the system from achieving its target angle. A misprediction in the fundamental frequency would cause the actuators to fire at inappropriate times, leaving residual energy in the rigid-body mode and the elastic mode. Imprecise placement of the actuators leads to inaccurately applied torques and forces that in turn would not accurately terminate the maneuver. The transient response of the actuators caused uncertainties in the equivalent pulse times associated with the prescribed impulses.

Certain dynamic characteristics were necessary to incorporate into the model. Both the actuator supply lines and instrumentation influenced the system stiffness. Although these effects were not modeled, they were taken into account by measuring the frequency of oscillation in the presence of a fully instrumented system with pressurized supply lines. The damping in the fundamental mode of vibration was also a necessary addition to the system model. The solution to the fuel-optimal slewing maneuver problem changed from a four-pulse solution to a three-pulse solution in the presence of damping. The problem of friction in the rotation hinge was minimized by appropriately skewing the beam's axis of rotation.

As was stated, measurement of the states was needed only for comparison with the analytical predictions. Errors in these states were due to sampling intervals, sensor noise, and modal

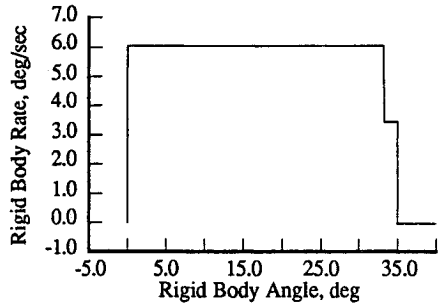

Fig. 10 Phase plane of rigid-body motion.

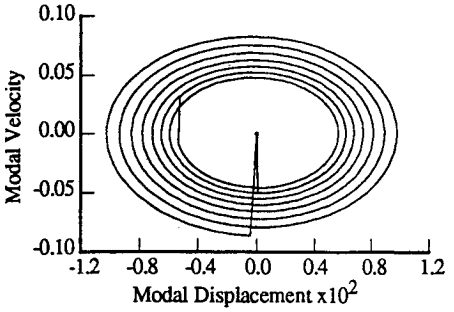

Fig. 11 Phase plane of elastic motion.

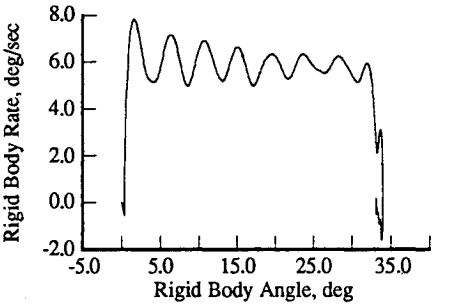

Fig. 12 Phase plane of rigid-body motion, experimental results.

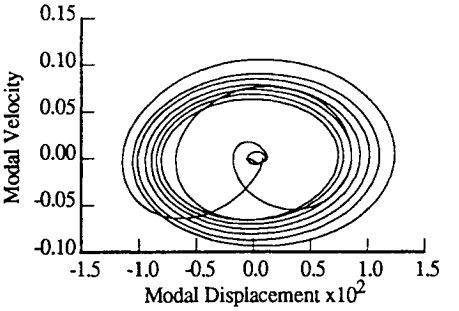

Fig. 13 Phase plane of elastic motion, experimental results.

filtering. Larger sampling intervals increased differentiation accuracy in the presence of sensor noise, yet smaller sampling intervals increased integration accuracy and resolution of the reconstructed impulse functions. This tradeoff led to a sampling interval of 0.01 s. Inaccuracies in the calculation of the system mass center led to residual components after modal filtering. This effect is seen in Fig. 12, where the elastic component of the response is still evident in the rigid-body rate, and in Fig. 13, where the magnitudes of the modal displacements and velocities are slightly higher than the analytical predictions.

Following the initial pulse, the measured slewing rate was 6.02 deg/s as compared with the predicted slewing rate of 6.05 deg/s. The measured slewing rate decreased due to hinge friction at the rate of 0.07 deg/s^2. At the termination of the maneuver, the beam slewed 34 deg instead of the predicted 35 deg. The ratio of residual vibration energy at the termination of the maneuver to the vibration energy immediately following the initial pulse was 0.396%.

Acknowledgments

Portions of this investigation were supported by the Mars Mission Research Center funded by NASA Grant NAGW-1331 and by NASA Langley Research Center under Contract NAG-1-977.

References

[1]Chukwu, E. N., *Stability and Time Optimal Control of Hereditary Systems,* Academic Press, New York, 1992.

[2]Silverberg, L., and Redmond, J., "Fuel-Optimal Reboost of Flexible Spacecraft," *Journal of Guidance, Control, and Dynamics,* Vol. 16, No. 2, 1993, pp. 294-300.

[3]Redmond, J., and Silverberg, L., "Fuel Consumption in Optimal Control," *Journal of Guidance, Control, and Dynamics,* Vol. 15, No. 2, 1992, pp. 424-430.

[4]Redmond, J., and Silverberg, L., "An Exact Solution to the Fuel Optimal Propulsive Control of a Tutorial Structure," *Journal of Sound and Vibration* (to be published).

[5]Sparks, D. W., and Juang, J., "Survey of Experiments and Experimental Facilities for Control of Flexible Structures," *Journal of Guidance, Control, and Dynamics,* Vol. 15, No. 4, 1992, pp. 801-816.

[6]Redmond, J., Meyer, J. L., and Silverberg, L., "Impulse Damping Control of an Experimental Structure," *Journal of Sound and Vibration,* Vol. 160, No. 1, 1993, pp. 179–186.

[7]Shenhar, J., Sparks, D., Jr., Williams, J. P., and Montgomery, R. C., "Attitude Control System Testing on SCOLE," *Proceedings of the Sixth Symposium on Dynamics and Control of Large Structures,* Virginia Polytechnic Inst. and State Univ., Blacksburg, VA, June 1987, pp. 251–273.

[8]Floyd, M. A., "Single-Step Optimal Control of the RPL Experiment," *Advances in the Astronomical Sciences,* Vol. 57, 1985, pp. 323–350.

[9]Silverberg, L., and Park, S., "Interactions Between Rigid-Body and Flexible-Body Motions in Maneuvering Spacecraft," *Journal of Guidance, Control, and Dynamics,* Vol. 13, No. 1, 1990, pp. 73–81.

[10]Meirovitch, L., *Computational Methods in Structural Dynamics,* Sijthoff and Noordhoff, Rockville, MD, 1980.

[11]Hale, F. J., *Introduction to Control System Analysis and Design,* Prentice-Hall, Englewood Cliffs, NJ, 1973.

[12]Silverberg, L., and Park, S., "Globally Optimal Maneuver of Distributed Systems," *Proceedings of the AIAA/ASME/ASCE/AHS/ASC 30th Structures, Structural Dynamics, and Materials Conference* (Mobile, AL), AIAA, Washington, DC, April 1989.